WIND TUNNEL TEST OF A SINGLE ELECTRICAL LIFT THRUST UNIT TO ASSESS STATIC AND DYNAMIC LOADS

Michele Zilletti, Davide Prederi, Roberta Costantini, Mirko Zaccara, Massimo Ricciardi
Leonardo Helicopters – Aircraft System Integration, Cascina Costa, Samarate (VA), Italy
Gabriele Morelli, Pierangelo Masarati
Politecnico di Milano, Dipartimento di Scienze e Tecnologie Aerospaziali, via La Masa 34, 20156 Milano Italy

Abstract

This paper focuses on the design of an experimental wind tunnel test rig to assess the static and dynamic loads generated by electrical lift thrust units in different flight conditions. Given the emerging interest of the aeronautical community in novel multi-propeller Electric Vertical Take-Off and Landing (e-VTOL) aircraft for Advanced Air Mobility, this paper aims to contribute to the definition of new methodologies and tools to assist the design since the early stages. More specifically, the study proposes an experimental setup to measure the static and dynamic loads along the three principal directions generated by an Electrical Lift Thrust Unit (e-LTU) to be used for comparison and correlation with simulation comprehensive tools. Due to the stiff propeller architecture, significant static and dynamic roll and pitch hub moments can be generated in some flight conditions, such as helicopter mode forward flight or conversion phase characterised by edgewise airflow. The same phenomenon is not normally observed in conventional articulated helicopter rotors in which the presence of the blade hinges reduces the moment hub loads.

1. INTRODUCTION

The introduction of electrical propulsion systems in rotary-wing aircraft has widened the aircraft design space to new vehicle architectures. Traditional aerospace industries and emerging companies have invested in developing Vertical Take-Off and Landing (VTOL) aircraft exploiting the advantages of distributed electrical propulsion systems. Researchers at NASA compared generic VTOL architectures encompassing relevant Urban Air Mobility (UAM) features and technologies, including propulsion architectures, highly efficient yet quiet rotors, and aircraft aerodynamic performance [1,2]. Some of the potential advantages offered by these architectures are an increased safety level due to the propulsion system's redundancy, no emissions for a fully electrical power system, and a reduced number of components of the drive system, which may lead to lower production and maintenance costs. One potential simplification of the propulsion system can be achieved by exploiting the presence of multiple lift/thrust units (LTUs), which can be used to provide differential thrust to control the aircraft avoiding the use of other traditional control mechanisms (e.g. swash plate and control chain, propeller blade pitch control, etc.).

Furthermore, given the wide operational speed and torque ranges of electrical motors, only a gearbox with few stages between the motor and the propeller may be required, leading to a significant weight saving compared to traditional combustion engine drive train systems. Finally, the fast response of electrical motors can be exploited to regulate the thrust of each LTU by controlling the RPM without the need to adjust the blade pitch angle as in traditional aircraft propellers or helicopter rotors' collective control. The RPM control may further simplify the LTU since stiff propellers can be used instead of articulated rotors, reducing the number of rotor components. Nevertheless, these new design features may open new challenges for designers in terms of control logic, propeller, hub, and airframe structural design, aeroelastic stability, and failure handling, which should be considered since the early design stages.

Articulated rotors are used in helicopters to achieve the primary control of the aircraft while reducing the dynamic loads transmitted to the rotor hub. Stiff propellers, instead, are expected to produce higher dynamic loads than traditional helicopter rotors due to the rigid connection of the blades to the rotor hub. In addition, the LTU is likely to operate at resonance frequencies of the vehicle due to the variable RPM control strategy, further amplifying the vibratory loads. Given this scenario, it is crucial to predict the static and dynamic loads generated by an LTU in different flight conditions, which will drive the design of the LTU itself, its supporting structure, and, consequently, the entire airframe.

Recently, researchers have tackled this problem both experimentally and numerically. Russell et al. [3] focused on modelling a small-scale LTU to determine the level of fidelity needed for accurate performance prediction. They used the helicopter comprehensive analysis tool CAMRAD II to correlate the wind tunnel test data relative to a single LTU. The analysis mainly focused on LTU performance rather than dynamic load prediction. Lately, NASA designed an ad-hoc wind tunnel test bed to assess the performance and the dynamic load generation of 6 LTUs supported by a beam structure [4,5]. The setup is fully reconfigurable since each LTU can be independently tilted and moved horizontally and vertically. Each LTU was equipped with a load cell to measure the six load components in the fixed reference frame. Sekula et al. [6] carried out a parametric study on the LTU transient response, validating analytical models against the experimental data obtained by NASA [5] and focusing on the importance of the rotor wake model and the elasticity properties of the blade. Shastry et al. [7] developed an analytical model to predict multi-rotor eVTOL structural loads focusing on transient and inharmonic wake interactions from multiple rotors. Staruk et al. [8] conducted a test on a full-scale 2-blade LTU (1.8 m diameter) in the wind tunnel observing high dynamic loads generated by the LTU in edgewise rotor airflow conditions.

In this paper, the design of a wind tunnel test rig aiming at dynamically characterising a single LTU in different flight conditions is discussed in Section 2. Section 3 describes the initial test carried out in the wind tunnel, while Sections 4 and 5 present a model developed using Leonardo Helicopter Division (LHD)'s GyroX3 aeroelastic in-house software and its initial numerical-experimental validation. Conclusions are drawn in Section 6 together with a future steps discussion.

2. TEST RIG DESIGN

This section presents the design of a single LTU wind tunnel test rig capable of measuring the six load components in the fixed reference frame at different wind speeds and LTU tilt angles. The main objective of this study is to validate a methodology to predict the static and dynamic loads of electrical LTUs without targeting a specific design. Therefore, off-the-shelf parts could be used for the test rig, minimising both time and budget.

The experimental tests were carried out at the LHD wind tunnel facility in Bresso, Italy. The tunnel is a closed-return, 2 m diameter by 2.5 m length single circuit, open jet test section type, with a contraction ratio of 5.18, equipped with a 400 kW – 1200 RPM electric motor and a ten constant-pitch blade fan (2.9 m diameter), which generates typical and max wind speeds of 50 and 65 m/s, respectively (unit length Reynolds number up to $4 \cdot 10^6\ 1/m$), with a turbulence factor 1.173%. The airstream quality is improved by installing turning vanes at each circuit corner and a single honeycomb at the settling chamber entrance. No heat exchanger is present, which limits operations up to 45° C. For this experiment, the maximum wind speed was 20 m/s.

Figure 1 shows a picture of the wind tunnel test rig, consisting of a pylon that supports the LTU assembly. The pylon allows adjusting the rotor disk angle of attack from 0 deg (helicopter mode) to 40 deg (where 90 deg would be aeroplane mode condition). The LTU propeller has a diameter of about 650 mm and is made of three fixed pitch blades clamped to a rigid hub. The blade flap and lag motions are inhibited at the blade root via a bolted connection; thus, the flap-lag movement is only allowed by the blade's flexible deformation. The blade characteristics such as inertia, stiffness, and sectional aerodynamics are not known. The blade has a highly tapered planform, with a moderate twist and a slightly swept tip. The hub consists of a metallic structure providing a high stiffness in both flap-wise and lag-wise directions. The rotor mast is stiffer than the blades and hub structure and is attached to the electrical motor via a bearing.

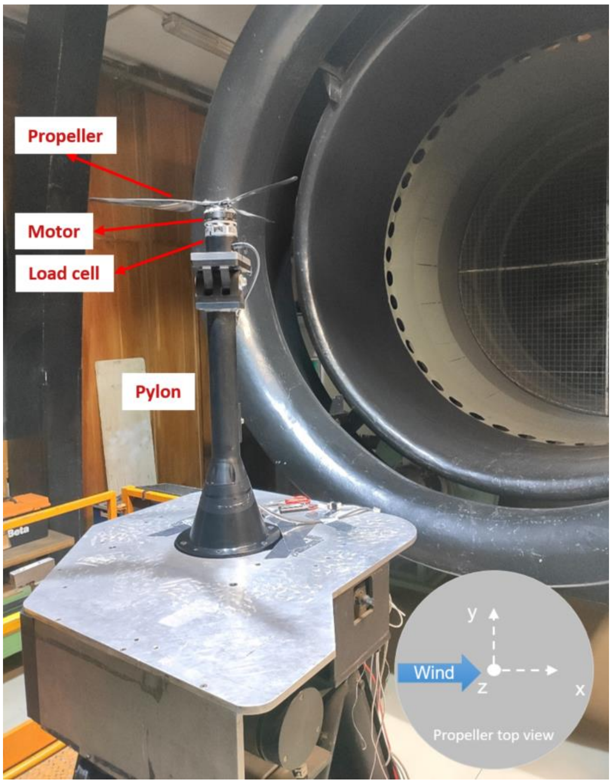

Figure 1: Wind tunnel test rig consisting of a supporting pylon structure and an LTU; system of reference (bottom right).

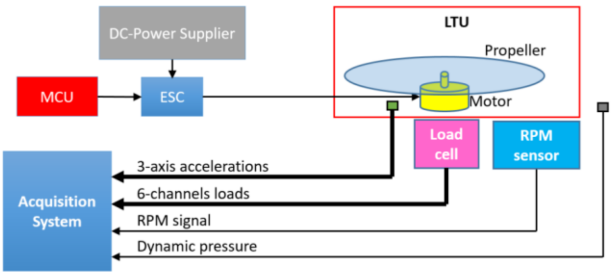

Figure 2: LTU, control electronic and acquisition scheme.

Figure 2 shows a schematic of the LTU with the electronic components used to drive the system and acquire the signals during the test. The motor is driven by an Electronic Speed Controller (ESC), which takes as an input the DC power voltage from a power supplier and a Pulse Width Modulated (PWM) signal generated by a Micro-Controller Unit (MCU). The PWM duty cycle, which controls the propeller's RPM, can be set via the MCU. A magnetic hall sensor is used to derive the rotational speed of the propeller by measuring the absolute angular position. The 6-channel load cell, located under the motor, outputs six signals used to calculate the three forces and moments generated by the LTU. A total of 11 signals, including the triaxial acceleration of the pylon measured at the load cell base and the dynamic pressure, are recorded via the acquisition system, which guarantees the necessary signal synchronisation.

2.1. Propeller characterisation tests

This subsection discusses the tests performed to identify the blade and propeller's static and dynamic properties. As previously pointed out, the propeller, hub, and motor are off-the-shelf components. Consequently, not all their physical parameters were known a priori. Identification tests were needed to estimate the unknown physical properties of the propeller used as input parameters of the aeroelastic model presented in the next section. Firstly, a 3D scan was performed to derive the blade geometry. The total blade mass, the centre of gravity (CG) position, and the moment of inertia were measured as well.

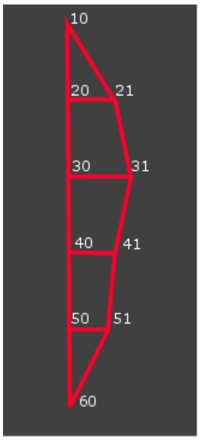

Figure 3: Measurement and excitation locations. Blade root at position 10.

As a second step, the blade dynamic properties were evaluated through a hammer test. A single blade was suspended via an elastic band characterised by a stiffness much lower than the blade's static stiffness to approximate free-free boundary conditions. An instrumented hammer was used to excite the blade at 10 locations scattered on the blade's surface, as shown by the scheme in Figure 3. A lightweight, single-axis microcharge accelerometer was placed at location 40. The position and orientation of the accelerometer were chosen among the possible candidate grid locations to maximise the observability of the modes. A hammer roving test was used to identify the blade resonance frequencies and their mode shapes. Table 1 summarises the first six modes, their type, normalised resonance frequency, and damping ratio.

Table 1: Blade modes' resonance frequency and damping ratio in free-free conditions, normalised to the 1st resonance value.

Mode	Type	Normalised Frequency	Damping ratio (%)
1	I beam	1.00	0.37
2	II beam	2.27	0.37
3	III beam	3.91	0.52
4	I torsion	4.18	0.66
5	IV beam	6.13	1.29
6	II torsion	6.81	0.78

2.2. Load cell dynamic characterisation

As the load cell is the only sensor measuring the loads generated by the LTU, it is crucial to select one able to measure both the static and dynamic forces and moments along the three principal directions in the fixed reference frame. A 6-axis extensometer load cell was used for this scope. The measurement is performed by directly measuring the deformation of the internal structure of the cell with six full bridge extensometers. The six measured deformations can be multiplied by a 6x6 calibration matrix to evaluate the six load components. One important aspect to be considered when dynamic measurements are required is the dynamic range of the cell, which is limited by the dynamic response of the load cell's internal structure. A test was carried out to characterise the dynamic behaviour of the load cell, which also accounts for the mass and inertia of the LTU. After installing the motor on the load cell (the rotor mass and inertia are negligible compared to those of the motor, so it was not installed), the frequency response function of the load cell was measured using a shaker.

A stinger, equipped with a single-axis piezoelectric load cell, connected the 6-axis load cell to the shaker. Figure 4 shows the Frequency Response Function (FRF) between the reference Fx input force measured by the piezoelectric load and the Fx component measured by the 6-axis load cell. The FRF for the other components were also measured; for the sake of brevity, they are not reported here.

As one can notice in Figure 4, the FRF has almost unitary magnitude and a nearly zero phase in the frequency region below 300 Hz. Since the expected maximum blade passing frequency for this LTU is below 300 Hz, one can conclude that the load cell can provide an accurate measurement by using the static calibration matrix provided by the supplier.

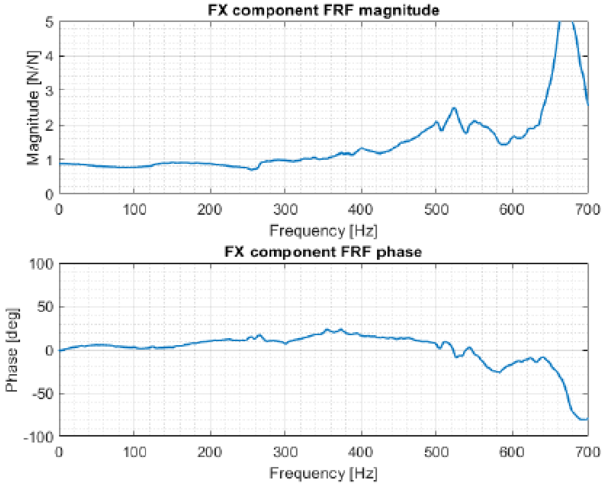

Figure 4: FRF between the input and load cell measured in plane x-axis force.

At higher frequencies, a peak around 670 Hz with a 90 deg phase shift indicates the presence of a resonance of the load cell structure, thus limiting the useful frequency measurement range.

A relatively stiff load cell structure must be selected to avoid resonance frequencies falling within the frequency range of interest for measurements. A stiff load cell structure implies that low deformations are expected, especially in some test conditions characterised by low load levels (low RPM and wind speed). Thus, if, on the one hand, a stiff load cell guarantees an adequate dynamic range, on the other hand, the cell may be working near its minimum measurable value with a potentially high noise-to-signal ratio. Consequently, the choice of the load cell was a trade-off between the frequency range and the measurement resolution.

2.3. Dynamic test of wind tunnel installation

The wind tunnel test rig, including the pylon, the load cell, and the LTU, was dynamically characterised to avoid structural resonances within the frequency range of interest for measurements. As such, a hammer test of the structure was carried out. Five 3-axis accelerometers were installed along the pylon while exciting the structure with an instrumented hammer. Figure 5 shows an FRF between the input force at the LTU location and the acceleration along the x and y-axes measured by a collocated accelerometer near the load cell base. The faint grey area on the graph shows the 3/rev expected frequency region (namely, the frequency of the expected loads transmitted by a three-blade rotor to its support). As one can notice, no resonances within the frequency range of interest may affect the load measurements during the test. Even if no resonances of the installation are expected to be excited, a 3-axis accelerometer was placed near the base of the load cell during the wind tunnel test for monitoring purposes.

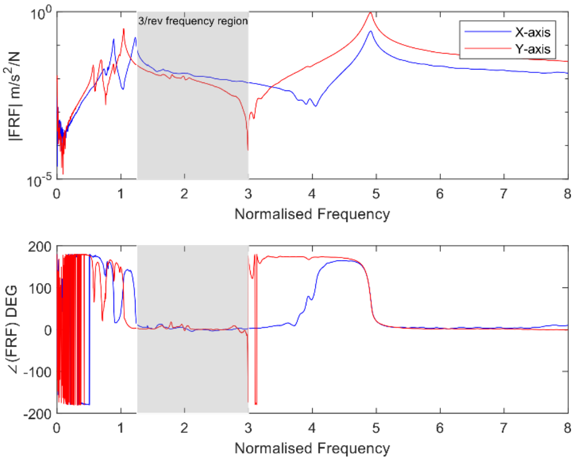

Figure 5: FRF between the hammer force and measured acceleration. The accelerometer is placed at the load cell base, and the force is imposed in the same direction as the measured acceleration (x blue line and y red line).

3. WIND TUNNEL ACQUISITION

For the test campaign, a matrix of 250 conditions, consisting of 5 wind speed conditions, 5 tilt angles, and 10 RPM steady-state regimes, as summarised in Table 2, were tested.

During the test, the following signals were acquired using the QuantumX acquisition system: 6-axis loads, the wind tunnel dynamic pressure, 3-axis accelerations of the pylon at the load cell base location, and the RPM. The acquisition was recorded after reaching steady-state wind speed and RPM conditions. Each acquisition lasted for 30 seconds with a sampling frequency of 6 kHz. Then, the signals were post-processed to obtain the static load component (i.e., the load time history mean values) and the harmonic component at the 3/rev frequency by computing the FFT of the measured signals. To allow a direct comparison between the test and simulation data, a common system of reference for the test and the simulation was used. The origin O is located at the hub centre, the x and z axis are aligned to the wind direction and the LTU thrust, respectively, and the y-axis is perpendicular to the wind direction to form a right-hand system of reference as shown in Figure 1.

Table 2: Wind tunnel condition test matrix.

Wind speed m/s	Tilting °	RPM (%)
0	0	0
8	10	14
12	20	28
16	30	42
20	40	56
		64
		78
		86
		97
		100

4. LIFT/THUST UNIT AEROELASTIC MODEL

An aeroelastic model of the LTU was built in GyroX3, an LHD in-house code [9]. The airfoil geometry was obtained via 3D blade scanning, and the related aerodynamic coefficients (i.e., lift, drag, and pitching moment) were defined as functions of the airfoil angle of attack and Mach number. To develop the look-up tables of the aerodynamic coefficients, a 2-D quadrilateral fully structured O-grid mesh was built with Pointwise ®, with boundary conditions of pressure far field on the external circular part and adiabatic wall boundary condition on the aerofoil surface. The SST k-ω turbulence models were used. The simulations were performed with Ansys Fluent® at Re/Ma = 6'256'000 (with unitary chord). The aerodynamic coefficients were then formatted using the C81 table standard.

Each blade is modelled using 22 beam elements with cubic shape functions, as shown in Figure 6 (the blue spherical markers represent the nodes between the beam elements). The three blades are connected to a shaft via three flexible beams representing the rotor hub. The shaft is modelled as a rigid element with one terminal connected to the rotor hub centre and the other end to the ground. Starting from the look-up tables obtained via CFD, the aerodynamic model for the aeroelastic simulation had to be chosen. Regarding the blade body, a Lifting Line modelling was preferred, with look-up tables used for the corrections of aerodynamic coefficients.

The rotor wake, instead, was modelled using a standard vortex panel wake. The blade aerodynamic mesh is made of 30 panels with geometrical progression (the mesh is finer in the tip region). Figure 7 shows a typical aerodynamic solution in hover with the first vortex rolling up and the near-wake narrowing just under the rotor plane.

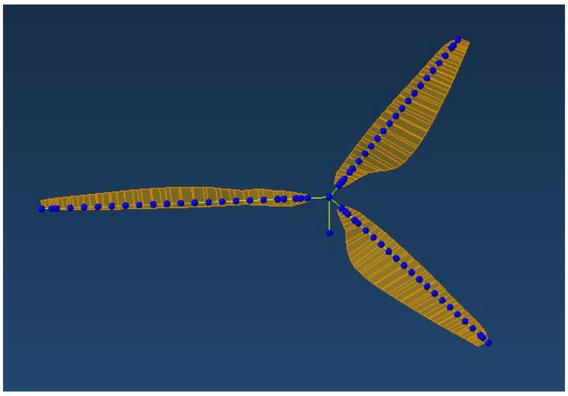

Figure 6: GyroX3 wind tunnel model.

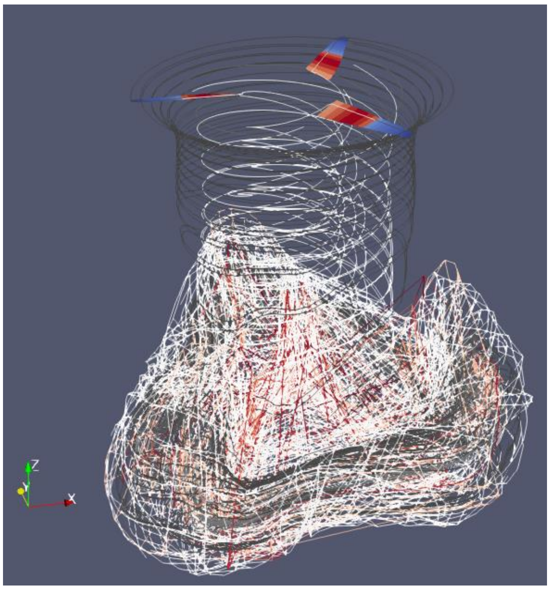

Figure 7: Aerodynamic solution in hovering.

5. SIMULATION AND MODEL CORRELATION

5.1. Rotor dynamic results

The results of the blade identification tests described in section 2.1 were used to tune the GyroX3 model parameters. The blade structure is discretised in 22 span-wise beam elements. The mass distribution of the blade was estimated based on the geometry derived from the 3D scan and an estimate of the material density. A span-wise density distribution was optimised to fit the overall CG position, the measured blade inertia, and the total blade mass. The cross-section moments of inertia were calculated from the geometry and mass distribution. Finally, Young's modulus and shear modulus were tuned to match the measured bending and torsional resonance frequencies of the blade in free-free conditions.

Table 3: % error between the first 6 measured and simulated free-free resonance frequencies.

Mode shapes	Experimental vs simulation % error
1st beam	-1.2%
2nd beam	-1.4%
3rd beam/tors	2.6%
1st torsion	5.4%
4th beam	1.3%
2nd torsion	-5.2%

Table 3 summarises the percentage error between the measured and simulated resonance frequencies. The model is able to capture the beam bending dynamics with an absolute error below 3%, while a slightly higher error, around 5%, can be noticed for the torsional blade dynamics. Overall, the model was able to predict with a satisfactory level of accuracy the first six resonance frequencies and modes shapes.

Once the isolated blade model was completed, the rotor model was assembled by connecting the three individual blades via three flexible beams representing the rotor hub. Since the hub stiffness was not known, an initial guess was used (ten times the static blade stiffness). The stiffness of the beam representing the hub was tuned based on wind tunnel test measurements to match the rotor speed at which an amplification due to the resonant response of the propeller was observed during wind tunnel tests, as discussed in the next section.

An alternative way to fit the hub parameters would have been to perform a hammer test of the entire propeller. However, this option was discarded for both technical and time constraint reasons. In fact, the test would have required a dedicated rig to constrain the propeller. Furthermore, the presence of the accelerometers may have affected the test results. Finally, the identification of the mode shapes and resonance frequencies could have been affected by the nonlinear dynamics introduced by the blade-hub constraints.

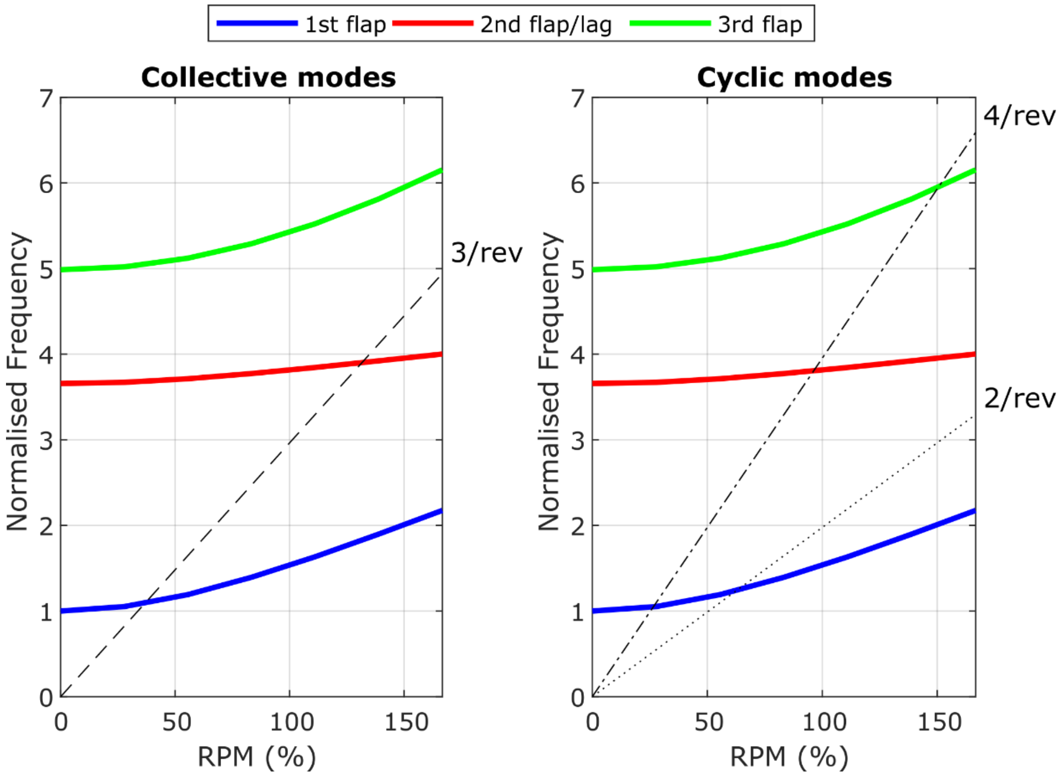

Figure 8: First three collective (left) and cyclic (right) normalised (to the 1st resonance) resonance frequencies of the propeller as a function of the RPM (%). The dotted, dashed and dashed-dotted lines represent the 2/rev, 3/rev, and 4/rev frequencies.

Figure 8 shows the first three simulated in-vacuum collective (left plot) and cyclic (right plot) normalised resonance frequencies of the propeller as functions of the RPM (%) with respect to a 1/rev rotating reference system. The blue, red, and green lines represent the resonance frequencies associated with the first beam bending mode, second coupled beam bending/chord-wise mode and third beam bending mode shapes, respectively. Finally, the 2/rev, 3/rev, and 4/rev frequencies are marked with the dotted, dashed, and dashed-dotted lines, respectively, as annotated on the right-hand side of the plots.

Even though all 2/rev, 3/rev and 4/rev excitation frequencies in the rotating reference system are generating 3/rev dynamic loads in the fixed frame, they excite different mode shapes and therefore contribute to different fixed frame load components, as summarised in Table 4. In particular, the 2/rev and 4/rev excite the cyclic modes, while the 3/rev excites the collective modes only. This means that the cyclic modes can generate amplification of the fixed frame 3/rev rotor in-plane load components, Fx, Fy, Mx, and My, while the collective modes are responsible for the amplification of the out-of-plane components Fz and Mz.

Table 4: Fixed frame load components amplified by the resonant propeller response at different RPM regimes.

Mode / Excitation	1st flap	2nd flap / lag	3rd flap
2/rev	Fx Fy Mx My 62 RPM (%)	-	-
3/rev	Fz 37 RPM (%)	Fz, Mz 132 RPM (%)	-
4/rev	Fx Fy Mx My 27 RPM (%)	Fx Fy Mx My 96 RPM (%)	Fx Fy Mx My 150 RPM (%)

As one can notice from the plot, the frequency lines cross the resonance lines multiple times, indicating that the propeller structure is excited at resonance at multiple RPM regimes.

It is worth highlighting that to avoid high loads, helicopter rotors, which operate at a single speed, are designed to avoid modal interactions with *n*/rev frequencies (where *n* is the number of blades); however, for variable RPM control of fixed-pitch rotors, maintaining an adequate clearance may not be possible.

The plot on the left of Figure 8 indicates that the first two resonances associated with the first and second collective mode shapes coincide with the 3/rev frequency at about 37 RPM (%) and 132 RPM (%), respectively.

Similarly, the plot on the right of Figure 8 shows that the first three resonances associated with the first three cyclic mode shapes (first flap, second flap-lag and third flap) coincide with the 4/rev frequency at 27, 96 and 150 RPM (%). Finally, the first cyclic resonances coincide with the 2/rev frequency at about 62 RPM (%).

Notice that the resonances at 27 and 37 RPM (%) are expected to induce a limited load amplification since the rotor speed is very low. Therefore, the potential critical speeds are 62, 96, 132 and 150 RPM (%). In particular, the collective resonance at 132 RPM (%) can mainly increase the 3/rev vibratory thrust, Fz; the cyclic resonances at 62, 96 and 150 RPM(%) are expected to mainly increase in-plane moments, My and Mx at the 3/rev frequency in the fixed frame.

5.2. Correlation results

Figure 9 shows the normalised measured (black lines) and simulated (red lines) static forces (left plots) and moments (right plots) as functions of the RPM; Figure 10 shows the corresponding dynamic loads at the 3/rev frequency. In these tests, the LTU tilt angle was set to 0 deg (helicopter mode) with a wind speed of 20 m/s. The plots show that measurements and simulated data are in reasonable agreement for static and dynamic loads. The minimum simulated RPM range starts around 50 RPM (%) because at lower RPM regimes the load levels (aerodynamic and inertial ones) are too low to be appreciated. Due to hardware limitations and safety reasons, the experimental acquisition was limited to 100 RPM (%).

Figure 9 shows that the thrust and torque are dominant static load components. Also, significant Mx and My components can be noticed due to the edgewise airflow conditions. Mx has a peak value

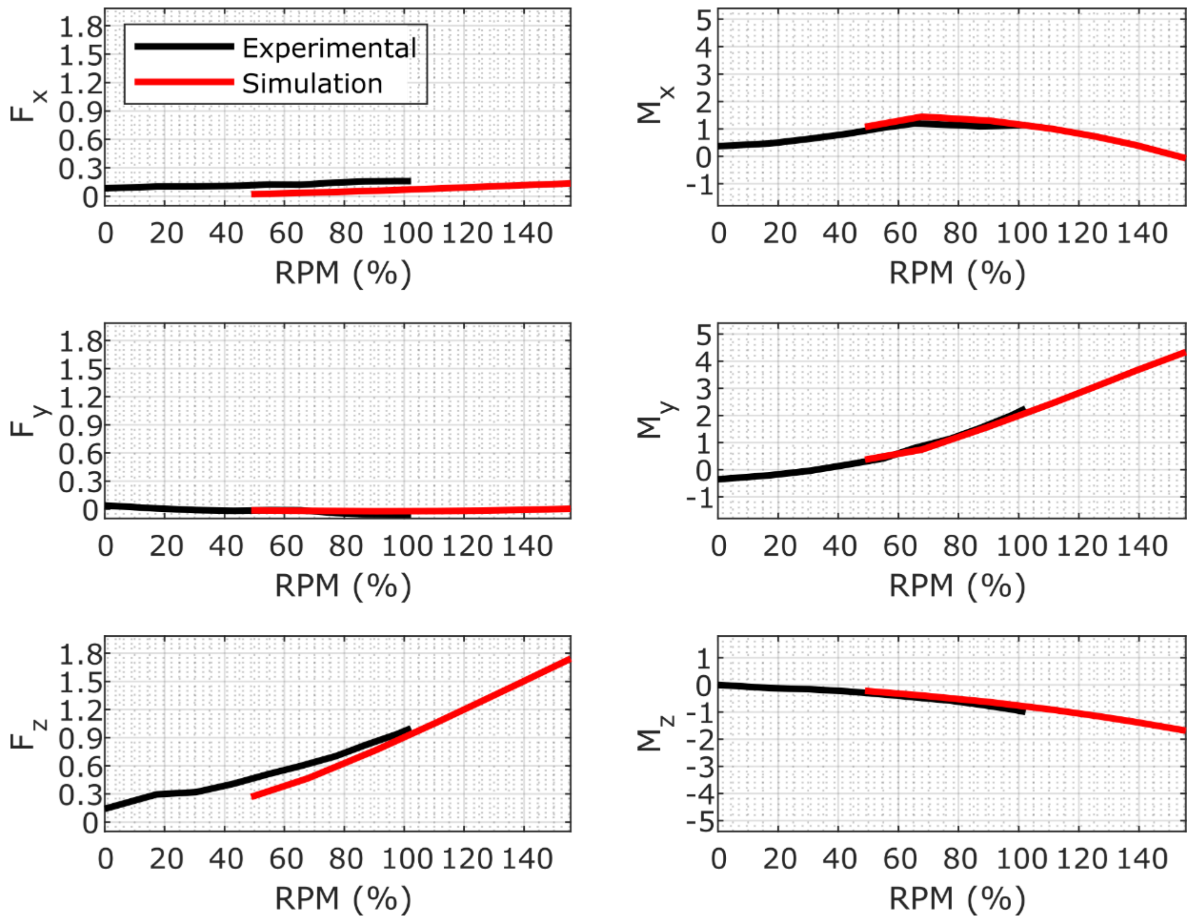

Figure 9: Measured (black line) and simulated (red line) static forces and moments as a function of RPM. Test condition: 0° tilt angle and 20 m/s wind speed. The forces and moments have been normalised to the static thrust and torque, respectively, measured at 100% RPM regime.

around 70 RPM (%) while My monotonically increases with the RPM. The static behaviour of both Mx and My is due to the elastic flapping of the blades (in particular, to the phase of flapping with respect to the forward speed).

The dynamic load components plotted in Figure 10 show a more complex pattern than the static loads. The observed dynamic load peaks can be explained by considering the rotor dynamic behaviour described by the fan plot in Figure 8.

As explained in section 5.1 and summarised in Table 4, some load components are expected to be amplified at certain RPM values. The 3/rev thrust peak at 40 RPM (%) is due to the propeller response of the first collective bending mode resonating at the 3/rev frequency. The rotor in-plane forces Fx and Fy and moments Mx and My peak at around 65 RPM (%) due to the propeller response of the first bending cyclic mode resonating at the 2/rev frequency in the rotating reference. This propeller resonance significantly increases the oscillatory Mx and My load components. Finally, the oscillatory torque component at about 140 RPM (%), only visible in simulation data, is due to the resonant response of the second collective mode. To better appreciate the level of dynamic moments' components, the solid line in Figure 11 shows Mx (top plots) and My (bottom plots) static components as functions of the RPM, while the shaded areas show the oscillatory ranges. The right-hand side plots are obtained from experimental data, while the left-hand side ones are obtained from simulation data. The plots show that at about 70 RPM (%) the propeller resonant response produces dynamic load components higher than their static counterpart.

These results show that high in-plane moments Mx and My can be generated by a rigid propeller exposed to edgewise airflow. Their oscillatory component is comparable in magnitude with the static one, potentially generating high vibration levels.

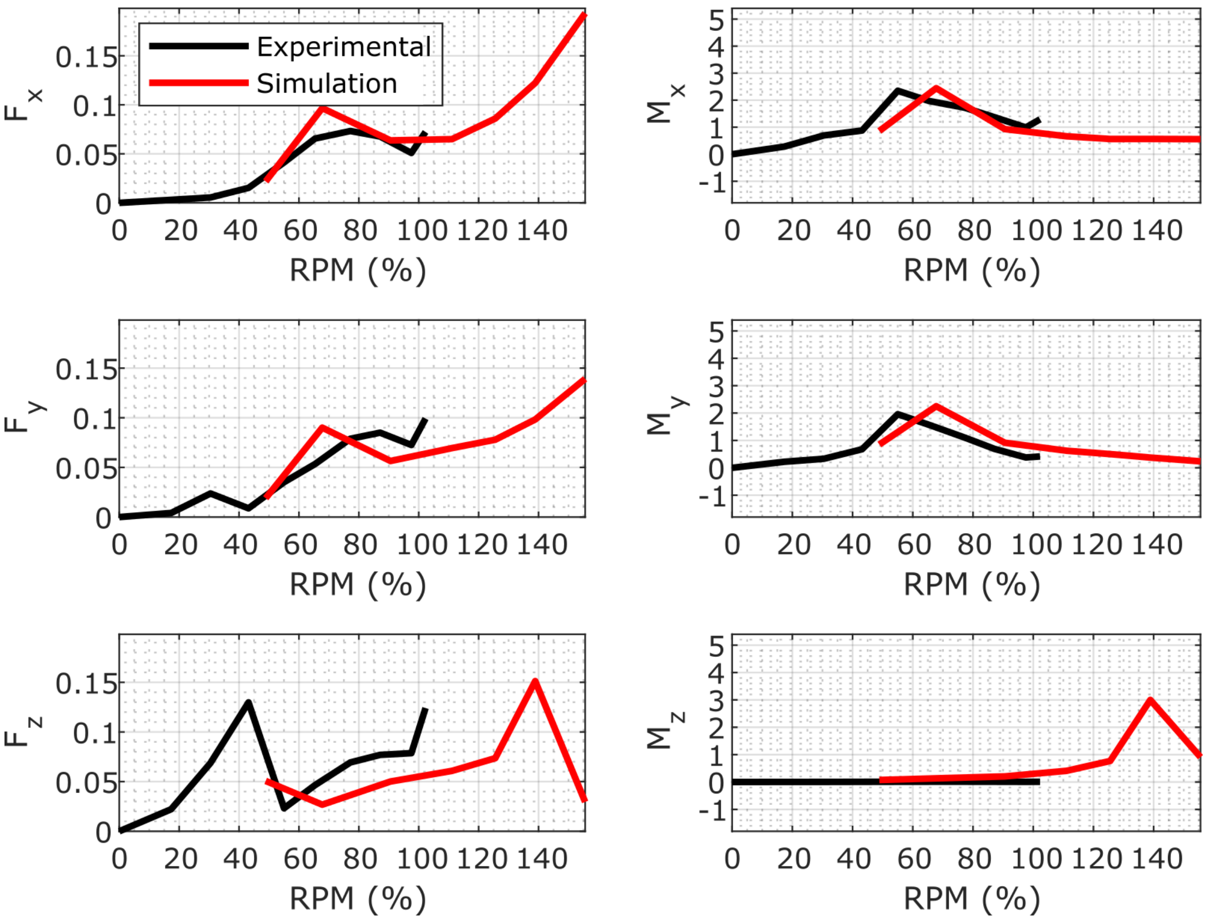

Figure 10: Measured (black line) and simulated (red line) dynamic forces and moments at the 3/rev frequency as a function of RPM. Test condition: 0° tilt angle and 20 m/s wind speed. The forces and moments have been normalised to the static thrust and torque, respectively, measured at 100% RPM regime.

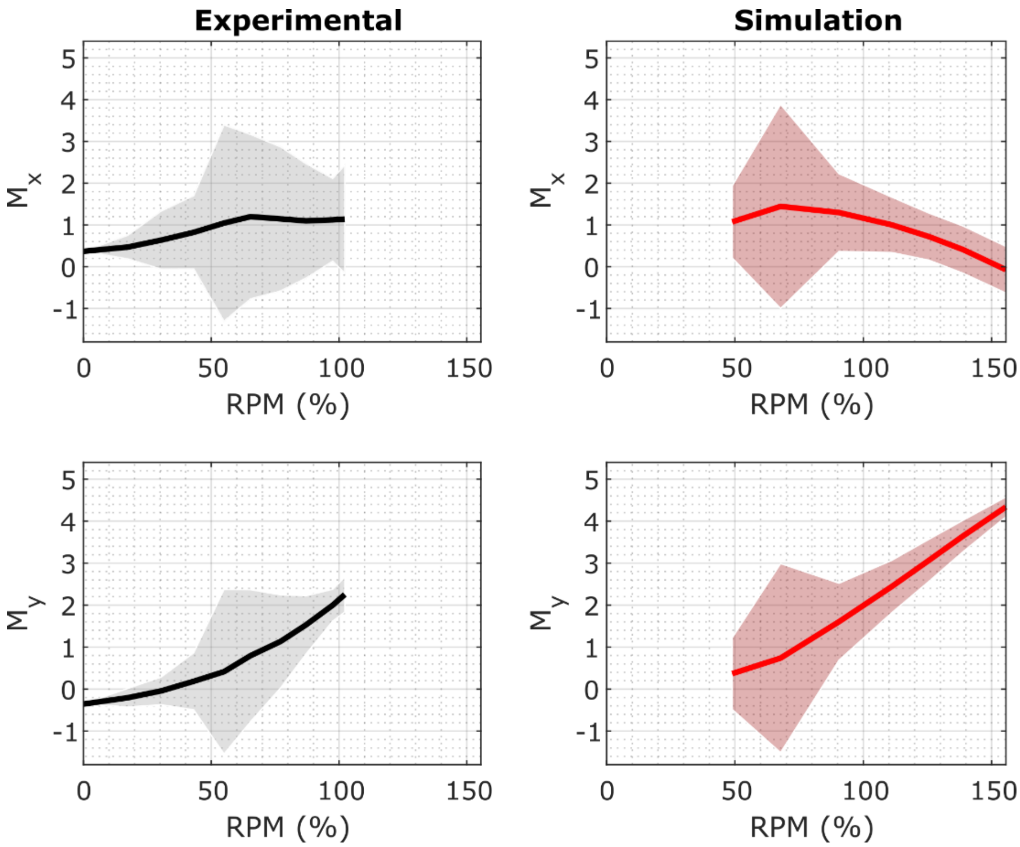

Figure 11: Mx (top plots) and My (bottom plots) components vs RPM. Static values (solid lines) and oscillatory range (shaded areas). Experimental data (left plots) and simulation data (right plots). The moments have been normalised to the static torque respectively measured at 100% RPM regime.

The high oscillatory moments may have a significant impact on both the sizing of the LTU and its maintainability. These aspects should be considered since the early design stage as they can significantly influence key features of the aircraft, such as control strategies, rotor design, and LTU installation.

5.3. Effect of LTU tilt angle on loads

This section analyses the effect of the tilt angle on the loads generated by the LTU. Firstly, the correlation between the measured and simulated static and dynamic loads at different airspeeds and tilt angles was assessed. The comparison showed that the aeroelastic model is able to simulate the static and dynamic behaviour of the LTU in different flight conditions with a reasonable level of accuracy. Considering the large number of conditions analysed, the complete set of results is not reported here for brevity; only the main conclusions are drawn. Once again, the most significant dynamic components in the presence of edgewise air flow are the rotor in-plane moments Mx and My, shown in the left and right plots of Figure 12 as functions of the RPM(%), tilt angle, and wind speeds. The plots show that the dynamic Mx and My components increase with the wind speed and decrease with the tilt angle. However, the peak due to the amplification caused by the resonant response of the rotor is still clearly visible in all test conditions. This result shows that particular care should be taken in designing the rotor and control laws to limit the vibratory loads and avoid unwanted vibrations and fatigue damage on the components. Due to the variable RPM, avoiding the rotor resonances in the entire flight envelope would be difficult. One mitigation to contain the vibratory loads would be to avoid stationary RPM regimes that excite the rotor at resonance. Furthermore, the conversion corridor shall be designed to avoid high forward flight speed conditions with low LTU tilt angles (helicopter mode). All these requirements, together with the overall aircraft control requirements, make scheduling the conversion corridor a challenging task.

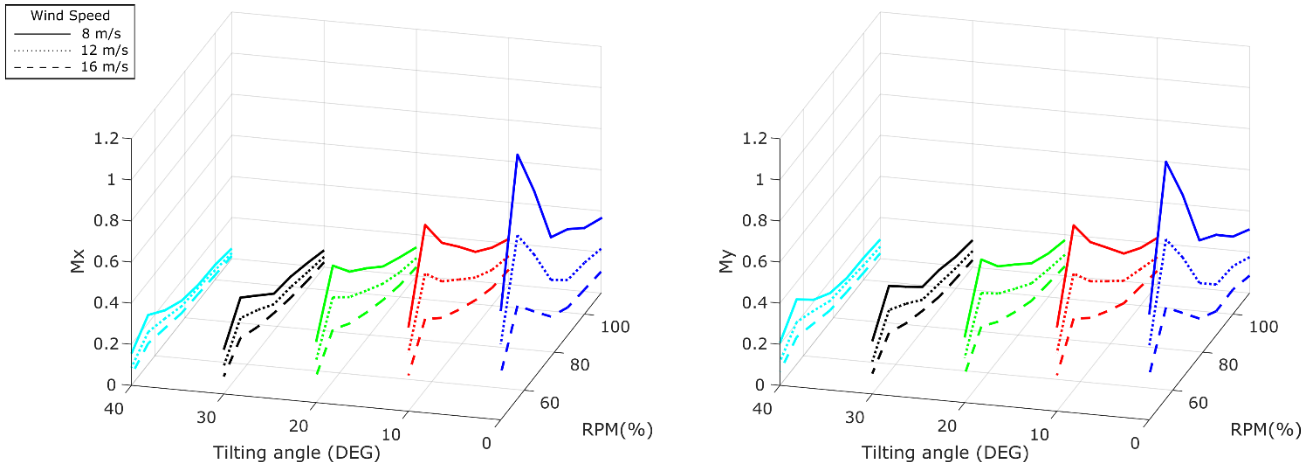

Figure 12: Normalised 3/rev Mx and My components as a function of tilt angle, RPM and wind speed condition.

6. CONCLUSIONS

This paper presented the initial results of the wind tunnel testing of an electrical LTU and their correlation with an aeroelastic model. A test setup was designed and built to characterise the static and dynamic behaviour of an electrical LTU.

The following conclusions can be drawn:

1. The test rig should be designed to avoid any intrusive dynamics of the installation or the sensors, which may affect the characterisation tests of the LTU.
2. An aeroelastic, free wake model implemented using GyroX3 proved to be able to simulate the static and dynamic behaviour of the LTU in different flight conditions with a satisfactory level of accuracy, compared to the wind tunnel test results.
3. The study showed that a stiff rotor can generate high oscillatory loads in edgewise air flow conditions, of magnitude comparable to that of the corresponding static load.
4. These significant dynamic load levels can impact the sizing and maintainability of the LTU.
5. The high vibratory loads shall be assessed in the early stage of the design as they may suggest the use of alternative design solutions (e.g., variable blade pitch, flapping or teetering blade hinges, LTU tilting, etc.)
6. The vibratory load components increase with the magnitude of the edgewise wind speed component and decrease when the LTU tilt angle moves from helicopter to aeroplane mode.

Future work will include simulation and testing of a single LTU in transient conditions and will feature multiple LTUs to study their interaction.

Author contact:

Michele Zilletti michele.zilletti@leonardo.com

7. REFERENCES

1. Johnson, W., and Silva, C. “NASA concept vehicles and the engineering of advanced air mobility aircraft,” *The Aeronautical Journal* Vol. 126(1295), 2022, pp. 59–91.

2. Silva, C., Johnson, W. R., Solis, E., Patterson, M. D., and Antcliff, K. R., “VTOL Urban Air Mobility Concept Vehicles for technology development,” AIAA Aviation Forum, 2018 Aviation Technology Integration, and Operations Conference, AIAA 2018-3847, Atlanta, Georgia, June 25-29, 2018.

3. Russell C. R. And Sekula M. K., „Comprehensive Analysis Modeling of Small-Scale UAS Rotors“ American Helicopter Society 73rd Annual Forum, Fort Worth, Texas, USA, May 2017.

4. Conley, S., “Multirotor Test Bed Load and Stress Analysis” NASA TM 20230000313, 2023.

5. Russell, C., & Conley, S., “The Multirotor Test Bed – A New NASA Test Capability for Advanced VTOL Rotorcraft Configurations“ Vertical Flight Society 78th Annual Forum Proceedings, Forth Worth, TX, May 2022.

6. Sekula, M. K., and C. R. Russell, "Time-Frequency Analysis of Experimental and Analytical Hub Loads of a Rotor Undergoing a Rotor Speed Change“, Vertical Flight Society 78th Annual Forum Proceedings, Forth Worth, TX, May 2022.

7. Shastry, A., and Datta, A., "Predicting Wake and Structural Loads in RPM Controlled Multirotor

Aircraft“ In Vertical Flight Society Aeromechanics for Advanced Vertical Flight Technical Meeting, San Jose, CA, January 2020

8. Staruk, W., Butt, L., Hennig, G., Bonny, E., Gray, C., Represa, D., and Toner, R, "Wind tunnel testing and analysis of a rigid, variable speed rotor for eVTOL applications.“ *Journal of the American Helicopter Society* 2023.

9. Sabatino, E., Prederi, D., Petri, F., Sciarappa, A., Cassinelli, C., Frassoldati, G., " Validation of a flexible and highly scalable mid-fidelity aerodynamic solver with wind-tunnel testing", Vertical Flight Society 79th Annual Forum Proceedings, West Palm Beach, FL, May 2023.